Nonlinear intensity dependence of photogalvanics and photoconductance induced by terahertz laser radiation in twisted bilayer graphene close to magic angle

S. Hubmann,[1] P. Soul,[1] G. Di Battista,[2] M. Hild,[1] K. Watanabe,[3] T. Taniguchi,[4] D. K. Efetov,[2] and S. D. Ganichev[1,5]

[1]*Terahertz Center, University of Regensburg, 93040 Regensburg, Germany*

[2]*ICFO-Institut de Ciencies Fotoniques, The Barcelona Institute of Science and Technology, Castelldefels, Barcelona 08860, Spain*

[3]*Research Center for Functional Materials, National Institute for Materials Science, 1-1 Namiki, Tsukuba 305-0044, Japan*

[4]*International Center for Materials Nanoarchitectonics, National Institute for Materials Science, 1-1 Namiki, Tsukuba 305-0044, Japan*

[5]*CENTERA Laboratories, Institute of High Pressure Physics, Polish Academy of Sciences, PL-01-142 Warsaw, Poland*

(Received 15 December 2021; accepted 28 January 2022; published 8 February 2022)

We report on the observation of the nonlinear intensity dependence of the bulk photogalvanic current and photoconductivity in the twisted graphene with small twist angles close to the second magic angle. We show that terahertz radiation results in photoresponses, which are caused by indirect optical transitions (free carrier absorption), direct interband transitions, and optical transitions between moiré subbands. The relative contribution of these absorption channels depends on the Fermi-level position with respect to the multiple moiré subbands of the twisted graphene. The interplay of these absorption channels results in oscillations of the photoresponses with variation of the gate voltage. We show that the photoresponse saturates at high intensities. For different absorption channels it has different intensity dependencies and saturation intensities. The latter depends nonmonotonically on the Fermi-level position, which is controlled by the gate voltage.

DOI: 10.1103/PhysRevMaterials.6.024003

I. INTRODUCTION

In the past decade, twisted bilayer graphene (tBLG) has been shown to be a promising and versatile material for fundamental research and applications. Several exotic states as tunble superconductivity and correlated insulators [1–9], emergent ferromagnetism [10], van Hove singularities [11,12], and twist-controlled tunneling [13] have been detected in tBLG. The material system is composed by two graphene sheets which are rotated with respect to one another by a specific twist angle θ. Consequently, a moiré superlattice is formed, and the value of the twist angle determines the size of the moiré unit cell, having crucial impact on the properties of the material system, for further references see, e.g., Refs. [14–35]. A special case arises if the twist angle θ is lower than 1°, where an extraordinary large moiré supercell is formed. In this case a highly complex energy spectrum consisting of several minibands is formed [15,30,35–37]. Such low-angle tBLG devices are in focus of the current research revealing some of the fascinating properties of this material system. However, there are only few works on optoelectronic phenomena in tBLG [37–43]. Most recently, we reported on the photogalvanic effects (PGEs) excited by low-intensity terahertz (THz) laser radiation in bulk and edges of tBLG [37]. This paper demonstrated that THz radiation results in a redistribution of carriers in momentum space caused by the asymmetric scattering in gyrotropic tBLG and provided evidence for the multitude of bands as well as the reduction of the symmetry of small-angle tBLG.

Here we report on the observation of the complex nonlinear intensity dependence of the THz radiation-induced PGE in small-angle tBLG. We show that the overall behavior of the photocurrent is crucially influenced by the applied backgate voltage U_G. The photocurrent exhibits pronounced oscillations with variations of U_G and its nonlinear behavior changes qualitatively: Depending on the backgate voltage the photocurrent shows linear behavior, saturate at high intensities, or even exhibits a change in sign with increasing radiation intensity. Furthermore, we observed the THz photoconductance, which shows sign-alternating oscillations with U_G and behaves nonlinearly with increasing radiation intensity. The observed oscillations are related to the resistance oscillations and are shown to be caused by the shifting of the Fermi energy across the multitude of moiré bands. The analysis demonstrates that the complex behavior of the photoresponse with increasing intensity is due to the interplay between two mechanisms of radiation absorption: Indirect optical transitions (Drude-like) give a contribution to the photoresponse as well as direct optical transitions between the moiré minibands. The obtained characteristics and the functional behavior of THz radiation saturation demonstrate that tBLG can be used for the development of THz mode-locking laser systems and detectors, which are already used in the infrared/visible spectral ranges applying monolayer graphene [44–51].

II. SAMPLES AND METHODS

A "cut and stack" method was used to assemble the hexagonal boron nitride (hBN)/tBLG/hBN/graphite heterostructure [20]. The graphene planes were first rotated by a target angle of 1 deg, and then the tBLG relaxed into the final twist angle of $\theta \approx 0.3$ deg. The stack was then etched

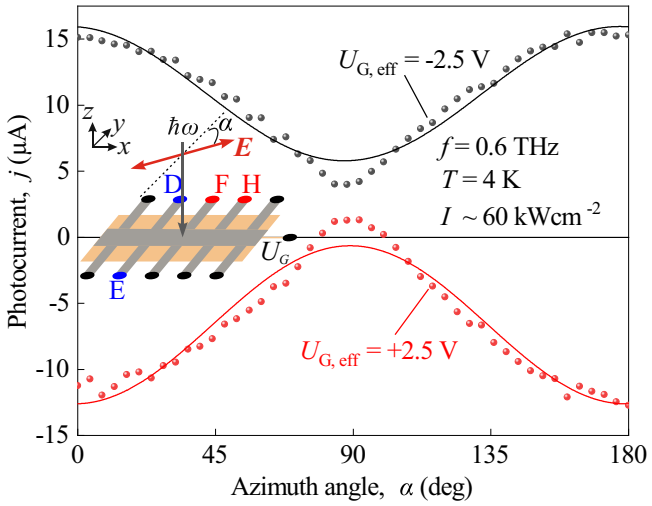

FIG. 1. Photocurrent as a function of the radiation electric-field orientation defined by the angle α at fixed backgate voltages of $U_{G,\mathrm{eff}} = \pm 2.5\,\mathrm{V}$ and a radiation frequency of 0.6 THz. The inset shows a sketch of the sample and defines the azimuth angle α. The data are fitted by Eq. (1) with fitting parameters j_0–j_2.

into Hall bar geometry ($4 \times 19\ \mu\mathrm{m}^2$), see the inset in Fig. 1, and one-dimensional contacts were made evaporating Cr/Au (5/50 nm) electrodes [52]. We define the directions along the long side of the Hall bar as the x direction, and perpendicular to that as the y direction. The tBLG was encapsulated between hBN layers and a graphite layer on the bottom was used as a local backgate. Bottom and top layers of hexagonal boron nitride (hBN) had a respective thickness of 18 and 13 nm as estimated from optical images.

Transport measurements were carried out in a He-4-based variable temperature insert cryostat in a temperature range from liquid helium to room temperature. We used a standard low-frequency lock-in technique to measure the resistance in two-terminal geometry with a 100-nA excitation current at a frequency of 12 Hz. To continuously tune the Fermi energy in our system we applied a gate voltage U_G in the range of ± 4 V to the graphite backgate. Note that for different sample cooldowns, the charge neutrality point (CNP) can occur at slightly different gate voltages. This is caused by, e.g., cooldown-dependent charge trapping in the insulator [53,54]. In order to account for this, below we use the effective gate voltage $U_{G,\mathrm{eff}} = U_G - U_{\mathrm{CNP}}$.

The THz electric field has been applied using a line-tunable pulsed high-power molecular gas laser [55,56], pumped by transversally excited atmospheric pressure CO_2-laser [57]. In this paper we used frequency lines of 0.6, 0.8, 1.1, 2, and 3.3 THz (photon energies of 2.5, 3.2, 4.4, 8.3, and 13.8 meV) with intensities up to a few $\mathrm{MW/cm^2}$, a pulse duration of about 100 ns, and a repetition rate of 1 Hz. The Gaussian-shaped laser beam was focused onto the sample using an parabolic mirror yielding a spot size of about 1.5 mm. Note that the size of the laser spot is much larger than the dimensions of the sample, which ensures an uniform illumination of the sample. The sample temperature has been controllably varied by using an optical continuous-flow cryostat, which allowed to tune the temperature between liquid-helium temperature and room temperature. Note that for the lowest temperature the sample was in liquid-helium bath and slightly pumped so that the temperature was about 4 K. The radiation intensity was modified using a crossed polarizer setup [58,59], and the radiation electric field was varied using half- and quarter-wave plates, see Ref. [60]. The rotation of the radiation electric-field $\boldsymbol{E}$ with respect to the y direction is described by the azimuth angle α, see the inset in Fig. 1. All experiments were conducted with a laser beam at normal incidence with respect to the sample surface.

The photocurrent is obtained in unbiased samples and is measured as a voltage drop along a load resistor $R_L = 50\,\Omega$ between different pairs of contacts across the Hall bar structure and along one side of the Hall bar structure. The latter measurements are important to conclude on the bulk or edge photocurrent origin. For the measurements of the photoconductivity the sample was additionally biased by a dc bias voltage $U_{\mathrm{dc}} = \pm 0.1$ V, and the photoconductive signal was measured in two-terminal geometry. In this kind of measurements, the signal consists of two contributions caused by the generation of the photocurrent and the change in conductivity upon irradiation. The former one is independent of the bias polarity, whereas the latter one changes its sign upon reversing U_{dc}. Using this fact, we extracted the photoconductivity signal from the photocurrent signals by subtracting the voltage drops obtained for positive and negative bias voltages and dividing by 2.

III. RESULTS

The illumination of the unbiased tBLG structure with linearly polarized THz radiation resulted in the emergence of a photocurrent measured across the sample (in the y direction, see the inset in Fig. 1). The photocurrent is detected in the whole temperature range studied here. Amplitude and sign of the photocurrent depend on the orientation of the radiation electric-field vector $\boldsymbol{E}$ and the value of the gate voltage. The polarization dependencies are exemplary shown in Fig. 1 for the contact pair D and E, a radiation frequency of 0.6 THz and two complementary gate voltages.

The dependence of the photocurrent on the azimuth angle α defining the orientation of $\boldsymbol{E}$ with respect to the y axis is described by [37]

$$j_y = j_0 - j_1 \cos(2\alpha) - j_2 \sin(2\alpha). \qquad (1)$$

This corresponds to a linear combination of the Stokes parameter P_0, $P_{L1} = \cos 2\alpha$, and $P_{L2} = \sin 2\alpha$ weighted by the coefficients j_0–j_2. Note that the contribution proportional to $P_{L2} = \sin 2\alpha$ is vanishingly small. Applying elliptically (circularly) polarization in the $\lambda/4$-plate setup we also detected a circular photocurrent contribution j_{circ}, which is proportional to the radiation helicity and reverses its sign by switching between right- and left-handed circularly polarized radiation. As addressed above, the photocurrent was observed across the sample only and was vanishingly small in measurements along the sample edges, e.g., along the contacts F–H, see the inset in Fig. 1. The overall behavior of the photocurrent reveals that it originates in the bulk PGE previously observed in Ref. [37] and is caused by the asymmetric scattering of photoexcited carriers in low-symmetric tBLG structures. The

TABLE I. Values of the parameters used for the fits of the data at $T = 4\,\mathrm{K}$ presented in Figs. 3 and 4.

Effective gate voltage, $U_{\mathrm{G,eff}}$ (V)	Frequency, f (THz)	A^{Dr} ($\mu\mathrm{A\,cm^2\,kW^{-1}}$)	$I_{\mathrm{s}}^{\mathrm{Dr}}$ ($\mathrm{kW/cm^2}$)	A^{ib} ($\mu\mathrm{A\,cm^2\,kW^{-1}}$)	$I_{\mathrm{s}}^{\mathrm{ib}}$ ($\mathrm{kW/cm^2}$)
−2.8	0.6	3.30	1.0	0.20	10.0
−2.2	0.6	0.36	5.0	0.18	25.0
−1.6	0.6	0.15	115.0	0	
−0.4	0.6	0.14	5.0	0.38	1.5
0.6	0.6	−0.67	64.0	0.87	7.6
1.0	0.6	−0.40	88.0	0.60	6.0
2.4	0.6	−0.14	79.6	0	
3.4	0.6	−0.10	65.0	0	
−2.5	1.1	0.56	2.5	0.18	1.4
2.5	1.1	−0.05	122.0	0	
−1.0	1.1	0.19	6.0	0.04	32.4

detailed discussion of the photocurrent formation is presented in Ref. [37] and, consequently, will not be discussed here.

Whereas the experiments in Ref. [37] were carried out applying radiation of the order of fractions of $\mathrm{W/cm^2}$, in the present measurements we used substantially higher (by about six orders of magnitude) intensities in order of tens of $\mathrm{kW/cm^2}$. As we show below, this drastic increase in radiation intensity results in a nonlinear behavior of the photocurrent.

Varying the voltage applied to the gate we observed oscillations of the photocurrent with $U_{\mathrm{G,eff}}$ at moderate radiation intensities of about $15\,\mathrm{kW/cm^2}$. These are observed at low temperature only and are shown exemplary for the polarization-independent photocurrent contribution j_0 in Fig. 2(a). The oscillation maxima are indicated by vertical arrows. The data are shown for different radiation frequencies, see Fig. 2(a) and the inset. The figure also shows the gate voltage dependence of the two-point resistance (gray line), demonstrating that the observed photocurrent oscillations correlates with those of the sample resistance. The photocurrent oscillations are caused by transitions between the multitude of moiré subbands and have the same origin as those observed at substantially lower intensity level (in the $\mathrm{W/cm^2}$ range) in Ref. [37]. The almost flat dispersion of the subbands results in sharp changes in the resistance with variation of the Fermi energy resulting in the filling and emptying of these bands. This process enables/disables direct optical transitions and modifies the Drude-like intraband absorption. Consequently, one obtains the oscillations of the photocurrent. Note that the photocurrent changes its sign in the vicinity of the CNP because of the sign change in the carrier charge.

Variation of the radiation frequency in the range from 0.6 up to 2 THz does not substantially change the gate voltage dependence of the photocurrent. This is shown in the inset in Fig. 2(a) where the photocurrent is shown normalized to their respective maximum value. The non-normalized data, exemplarily shown for $U_{\mathrm{G,eff}} = -2.2\,\mathrm{V}$ are plotted in Fig. 10. The figure demonstrates that the signal magnitude substantially increases with decreasing frequency [61].

Strikingly, a substantial increase of the radiation intensity does not change the photocurrent magnitude much. This demonstrates the nonlinear behavior of the photocurrent. Furthermore, the increase in radiation intensity modifies the gate voltage dependence, see Fig. 2(b). Whereas the oscillations are still resolved, they become less pronounced and frequency dependent, see the insets in Fig. 2. The former observation reveals that the nonlinearity changes with the gate voltage.

In order to study the nonlinearity, we investigated the intensity dependence of the photocurrent. Figure 3 shows the corresponding dependencies of the photocurrent obtained at several gate voltages. The figure demonstrates the complex behavior of the photocurrent with the increase in the radiation intensity and reveals that the nonlinearity type depends on the gate voltage. Whereas for most gate voltages the current saturates with rising intensity, see Fig 3(a), for low positive gate voltages close to the oscillation extrema, the photocurrent exhibits a change in sign with increasing intensity, see Fig. 3(b). Figure 4 shows that at an increase in temperature up to about 100 K, the photocurrent changes neither the magnitude nor the nonlinearity. Measuring the photocurrent and the two-point resistance at room temperature we observed that the oscillations with the gate voltage disappear. The photocurrent is almost constant for high gate voltages and changes its sign at the CNP. This is shown for different photocurrent contributions in Fig. 5. Note that the contributions j_0 and j_1 were extracted by measuring the dependence of the photocurrent on the gate voltage for $\alpha = 0^\circ$ and $\alpha = 90^\circ$, and calculating the half-sum (j_0) or half-difference (j_1) of the corresponding photocurrents, respectively. Similarly, the circular contribution was extracted by taking the half-difference of photocurrents excited by right- and left-handed circularly polarized radiation. Studying the intensity dependence for room temperature, we observed that the photocurrent saturates, whereas the saturation intensity increases strongly (not shown).

To obtain a complete picture of the observed nonlinearity, we studied the radiation-induced change of conductivity $\Delta\sigma/\sigma$.

Figure 6 shows the gate voltage dependence of $\Delta\sigma/\sigma$ measured for different frequencies. The non-normalized gate voltage dependence of the corresponding signal magnitude is shown in Fig. 10 in the Appendix. As addressed above the photoconductivity is extracted from the response in the biased sample by taking the half-difference between the photosignals obtained for positive and negative bias voltages. In order to simplify the comparison between the photoresponse for different frequencies in Fig. 6, we normalized the photoconductivity on its maximum values obtained at

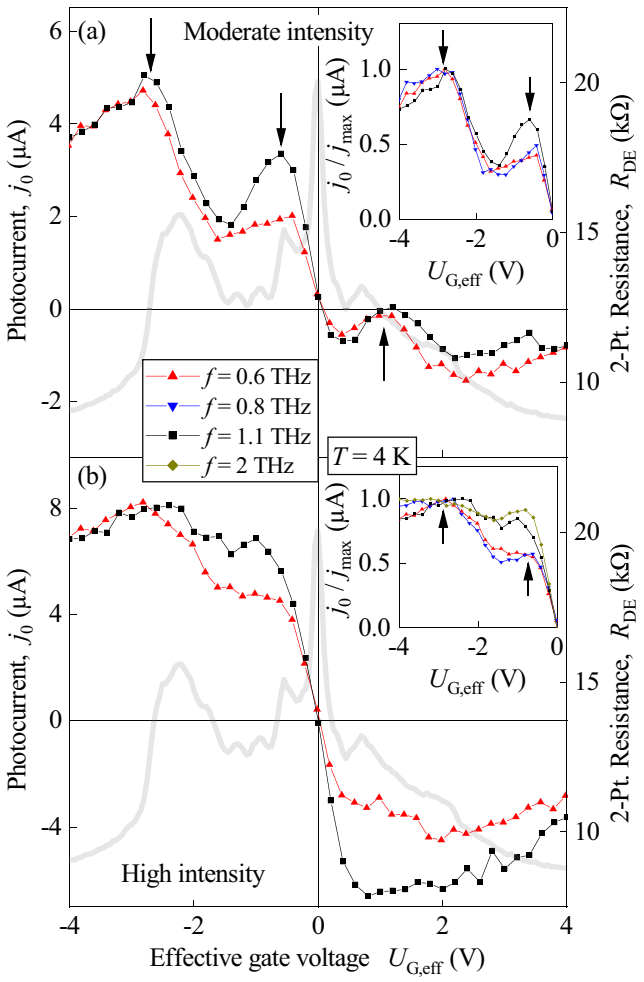

FIG. 2. Dependences of the polarization-independent photocurrent contribution [Eq. (1)] for the y direction (see the inset in Fig. 1) on the effective backgate voltage $U_{G,eff}$ for different radiation frequencies. The thick gray line shows the corresponding two-point resistance R_{DE}. The insets show a zoom-in of the corresponding dependencies for negative gate voltages and more radiation frequencies. Note that the data in the insets are normalized to their respective maximum value. The corresponding radiation intensities in panel (a) are as follows: 15 kW/cm^2 (0.6 THz), 15 kW/cm^2 (0.8 THz), and 20 kW/cm^2 (1.1 THz), The radiation intensities in panel (b) are as follows: 60 kW/cm^2 (0.6 THz), 170 kW/cm^2 (0.8 THz), 190 kW/cm^2 (1.1 THz), and 1100 kW/cm^2 (2 THz). Note that the corresponding radiation intensities in (b) are by orders of magnitude higher than in (a).

$U_{G,eff} = -2.3$ V. Note that the maximum of the photoconductivity coincide with an oscillation maximum of the sample resistance, see Fig. 6. The photoconductivity signal exhibits pronounced sign-alternating oscillations with the gate voltage, which, alike the photocurrent, correlates with the resistance. Note that, whereas the resistance exhibits pronounced oscillations, its magnitude does not change much. Therefore, peaks are clearly present in the gate voltage dependencies of both $\Delta\sigma/\sigma$ and photoconductive signal, see Figs. 6 and 9, and normalization only slightly reduces the maxima amplitudes.

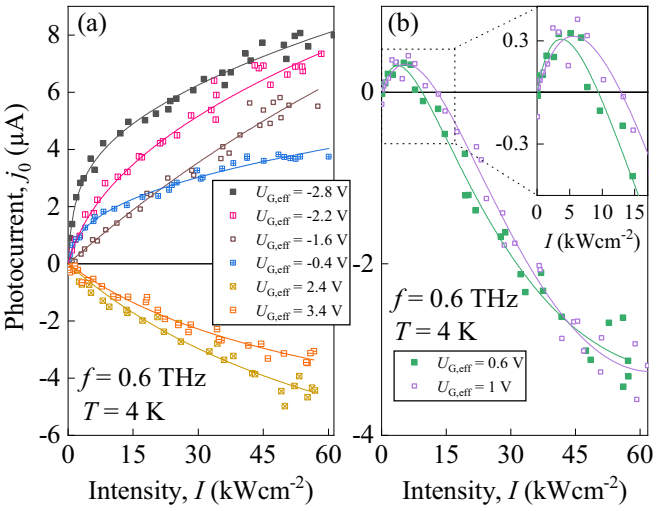

FIG. 3. Dependences of the polarization-insensitive photocurrent contribution in the y direction (see the inset in Fig. 1) on the radiation intensity I at a radiation frequency of 0.6 THz for different effective gate voltages. The inset in panel (b) shows a zoom-in for low intensities as emphasized by the dashed rectangle. The curves show fits according to Eq. (4). The corresponding fit parameters are given in Table I.

Importantly, the oscillations are detected even at highest intensities and because of the change in sign are pronounced even better. Furthermore, in contrast to the photocurrent, the photoconductive signal does not change its sign in the vicinity of the CNP. Note that the photoconductivity signal shows only a slight dependence on the orientation of the radiation electric-field $\boldsymbol{E}$ (not shown). Studying the intensity dependence of the photoconductivity we observed that for all gate voltages it saturates with the increase of intensity. The intensity dependence is exemplary shown in the inset in Fig. 6 for

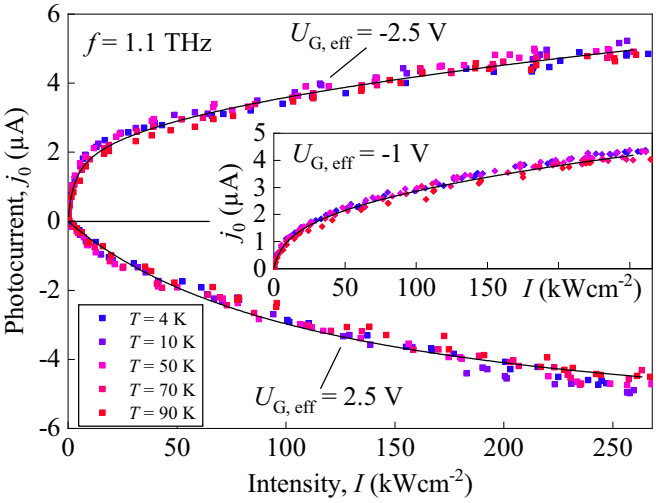

FIG. 4. Dependences of the polarization-independent photocurrent contribution in the y direction (see the inset in Fig. 1) on the radiation intensity for different gate voltages and various temperatures. The curves show fits according to Eq. (4). The corresponding fit parameters are given in Table I.

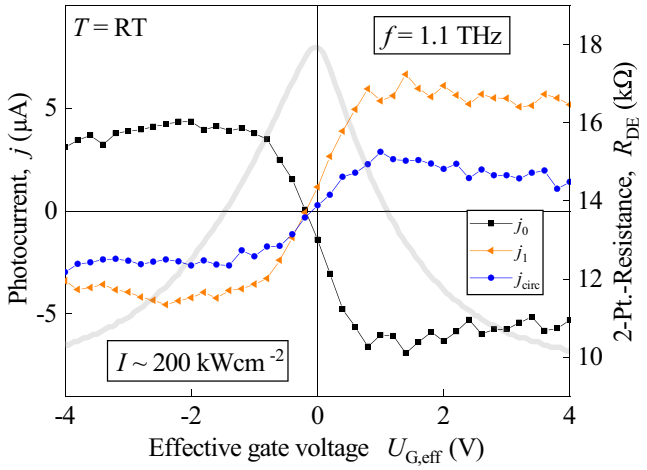

FIG. 5. Dependences of the photocurrent contributions j_0, j_1, and j_{circ} [see Eq. (1) for the y direction] (see the inset in Fig. 1) on the effective backgate voltage $U_{\mathrm{G,eff}}$ for room temperature. The thick gray line shows the corresponding two-point resistance R_{DE}.

an effective gate voltage of -2.3 V at radiation frequencies of 0.6 and 1.1 THz. Whereas the unity-normalized, relative photoconductivity curves as a function of the gate voltage essentially coincide for different frequencies, the signal magnitudes substantially depend on the radiation frequency. The inset in Fig. 6 shows that the decrease in frequency results in a strong increase in the photoconductivity amplitude.

An increase in the sample temperature results in a qualitative change in the effective gate voltage dependence, see Fig. 7. At high temperature ($T \geqslant 90$ K) the formerly observed

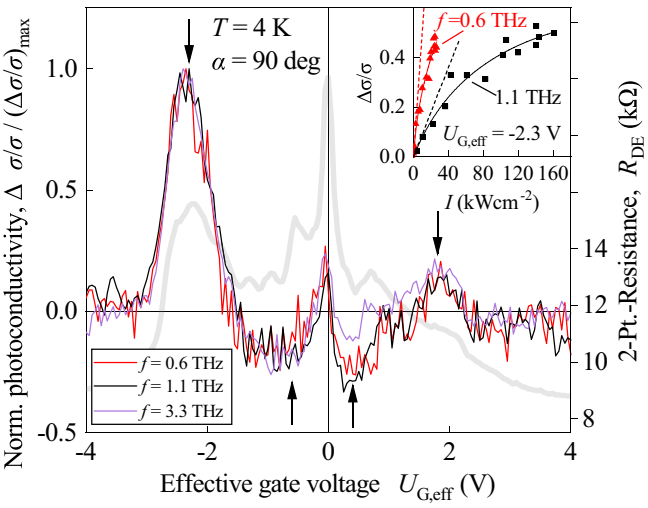

FIG. 6. Dependences of the photoconductivity $\Delta\sigma/\sigma$ in the y direction (see the inset in Fig. 1) on the effective gate voltage $U_{\mathrm{G,eff}}$ for different radiation frequencies. The curves are normalized to their maximum value. The thick gray line shows the corresponding two-point resistance R_{DE}. The corresponding radiation intensities are 45 kW/cm^2 (0.6 THz), 200 kW/cm^2 (1.1 THz), and 380 kW/cm^2 (3.3 THz). The inset depicts the intensity dependences of the photoconductivity $\Delta\sigma/\sigma$ as a function of the radiation intensity for $U_{\mathrm{G,eff}} = -2.3$ V and radiation frequencies of 0.6 and 1.1 THz.

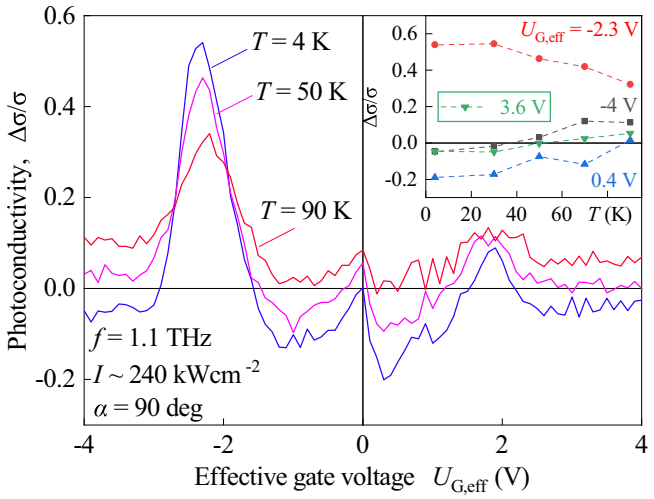

FIG. 7. Dependences of the photoconductivity $\Delta\sigma/\sigma$ in the y direction (see the inset in Fig. 1) on the effective gate voltage $U_{\mathrm{G,eff}}$ for different temperatures at a radiation frequency of 1.1 THz. The corresponding radiation intensity is 240 kW/cm^2. The inset shows the dependences of the photoconductivity at various gate voltages as a function of the temperature.

changes in photoconductivity sign are not present, whereas the oscillations are still clearly detected. The inset in Fig. 7 shows the dependence on the photoconductivity measured at $U_{\mathrm{G,eff}} = -2.3$ V at which the photoconductivity approaches its maximum and three traces at different gate voltages as examples of the temperature-dependent sign inversion.

IV. DISCUSSION

A. Nonlinear photogalvanic current

As addressed above the observed photocurrent described by Eq. (1) is caused by the bulk photogalvanic effect. The microscopic theory of this photocurrent is presented in Ref. [37]. It reveals that the three photocurrent contributions, which are given by the coefficients j_0–j_2 and the corresponding Stokes parameters, are caused by the electron scattering asymmetry of the photoexcited carriers and are proportional to the radiation absorbance η. The latter determines the variation of the photocurrent with the radiation intensity, see, e.g., Refs. [44,45,47–51,59,62,63]. In the considered twisted graphene structures, absorption of THz radiation with photon energies of the order of several meV can, in general, be caused by two mechanisms: The free-carrier absorption due to indirect *intra*band optical transitions (Drude-like) and the direct *inter*band/*intersub*band optical transitions [64].

Figure 3(a) shows that for most gate voltages the photocurrent saturates with increasing radiation intensity. For the studied range of radiation intensities absorption bleaching is indeed the most favorable nonlinear process for both absorption mechanisms [59,62,63] because other effects, which may cause the nonlinear absorption, such as, e.g., two-photon absorption, require much higher intensities to yield a contribution comparable to the one-photon absorption channel [59]. The bleaching of the Drude-like radiation absorption in monolayer graphene has recently been observed by means

of nonlinear ultrafast [65] and nonlinear photogalvanic THz spectroscopy [59]. The range of radiation frequencies (0.4–1.2 THz) and electric fields (2–100 $\mathrm{kVcm^{-1}}$) used in these studies are similar to those used in our paper. It has been shown that the absorption bleaching is caused by electron gas heating followed by energy relaxation and is well described by the empirical analytical formula,

$$\eta^{\mathrm{Dr}} \propto \left(1 + \frac{I}{I_s^{\mathrm{Dr}}}\right)^{-1}, \tag{2}$$

with the saturation intensity I_s^{Dr} being proportional to the reciprocal energy relaxation time and the Drude absorption cross section. Absorption and saturation of the photogalvanic current for direct optical transitions have been theoretically and experimentally studied in monolayer graphene, see Ref. [59]. The theory developed for the Dirac energy dispersion yields that at high intensities the absorption varies with the radiation intensity as [66,67]

$$\eta^{\mathrm{ib}} \propto \left(1 + \frac{I}{I_s^{\mathrm{ib}}}\right)^{-1/2}, \tag{3}$$

where I_s^{ib} is the corresponding saturation intensity. Such functional behavior is also known for the inhomogeneous model of direct optical transitions [68,69]. For the complex band structure of tBLG with a twist angle close to the magic angle, these theories cannot be directly applied and the required analytical equation is not developed as yet. Nevertheless, as we show below, Eq. (3) together with Eq. (2), describes well all experimental findings.

We begin with the polarization-independent contribution j_0, which yields the dominant contribution to the bulk photogalvanic current, see Fig. 1. We assume that the total photocurrent to be caused by an interplay of the photogalvanic current related to the absorption due to indirect and direct optical transitions, whose nonlinear behavior is described by the equations above. Consequently, the total photocurrent is given by

$$j_0 = A^{\mathrm{Dr}} I \left(1 + \frac{I}{I_s^{\mathrm{Dr}}}\right)^{-1} + A^{\mathrm{ib}} I \left(1 + \frac{I}{I_s^{\mathrm{ib}}}\right)^{-1/2}, \tag{4}$$

with fitting parameters A^{Dr}, I_s^{Dr}, A^{ib}, and I_s^{ib}. Here A^{Dr} and A^{ib} are low-intensity amplitudes of the PGE caused by indirect and direct optical transitions, respectively. Corresponding fits are shown in Fig. 3 demonstrating that the equation describes well the experimental data. Fitting parameters used for calculation of these curves are given in Table I. The nonlinearity of the linear and circular photogalvanic effects given, respectively, by the coefficients j_1 and j_c are also well described by Eq. (4) (not shown) [70]. Therefore, to be specific, below we focus our discussion on the nonlinearity of the polarization-independent contribution j_0.

Fitting the data for different gate voltages we observed that all fitting parameters vary non-monotonically, see Table I. First, we discuss the amplitudes of the photocurrents excited due to indirect and direct optical transitions. Table I shows that the amplitude A^{Dr} of the photocurrent caused by the Drude absorption changes the sign by switching from positive to negative gate voltages, i.e., it has opposite polarity for electron and hole conductivity. This is a direct consequence of the PGE current, which in the absence of an external magnetic field is described by an odd function of the carrier charge [59]. Microscopically, this photocurrent is generated due to asymmetric scattering of electrons driven back and forth by the THz field. Both radiation absorption and scattering asymmetry depend on the details of the band structure. In the studied twisted graphene the THz radiation-induced photocurrent is formed due to indirect optical transitions in one of the moiré bands. Consequently, for different gate voltages, i.e., different Fermi-level positions, it is generated in different moiré bands. Calculations of the band structure show that these bands are characterized by very different energy dispersions [15,30,35–37], and, therefore, it is not surprising that the coefficients A^{Dr} for various gate voltages differ by several times.

For the direct optical transitions, the highest values of the coefficients $A^{\mathrm{ib}} > 0$ are obtained for the gate voltages corresponding to the CNP vicinity, see Table I. This photocurrent is attributed to the direct interband transitions resulting in the generation of the electron-hole pairs followed by asymmetric scattering. Its amplitude depends on the difference in occupation of the initial and final states of the optical transitions. The sign of this current is only defined by the difference of the electron and hole momentum relaxation times and does not change by switching from electron to hole conductivity. Note that for the positive gate voltages the amplitude A^{ib} is positive, whereas A^{Dr} is negative, and, therefore, for the photocurrent extremum at $U_{\mathrm{G,eff}} = 1\mathrm{V}$, see vertical arrow in Fig. 2(a), these currents almost completely compensate each other, and, thus, the total current becomes zero. The photocurrent due to the direct interband transitions is generated in the vicinity of the CNP and vanishes at higher positive/negative gate voltages. At large negative gate voltages (about -2.5 V), however, we observed that the direct optical transitions yield a considerable contribution to the total photocurrent, see Table I. At these $U_{\mathrm{G,eff}}$'s the Fermi level is located in the gap between two moiré subbands, which corresponds to the highest difference in occupations of initial and final states, and enables direct optical transitions between these bands. Consequently, we obtain the peak of the photocurrent and the maximum of the sample resistance, see the vertical arrow in Fig. 2(a). Outside the peak amplitudes, A^{ib} decreases and approaches zero.

The most clear evidence for the presence of two competing mechanisms of the photocurrent, which are caused by indirect and direct optical transitions characterized by different saturation intensities, comes from the results obtained for low positive gate voltages. Indeed, in most of the cases we observed that for negative gate voltages the total photocurrent j_0 has a positive sign in the whole range of used radiation intensities, and for positive gate voltages its sign reverses, see Fig. 3(a). For low positive gate voltages, however, we detected that an increase in the radiation intensity results in the photocurrent sign inversion, see Fig. 3(b). For low gate voltages, being close to CNP, the contribution of the indirect optical transitions to the photocurrent is small because these voltages are close to the sign inversion at the CNP at which A^{Dr} vanishes due to the sign inversion. Consequently, the photocurrent is dominated by the interband mechanism ($A^{\mathrm{ib}} > |A^{\mathrm{Dr}}|$), which results in a positive photocurrent sign, see Table I. An increase in the radiation intensity, however,

results in the saturation of this mechanism with $I_s^{ib} < I_s^{Dr}$, see Table I, and the Drude contribution to the photocurrent shows up. The latter one has a negative sign and, respectively, the sign of the total photocurrent changes. Fitting functions in Fig. 3(b) show that the above scenario indeed describes well the complex intensity behavior observed for low positive gate voltages.

Now, we discuss the variation of the saturation intensities with the gate voltage. As addressed above, both I_s^{Dr} and I_s^{ib} vary nonmonotonically with $U_{G,eff}$, see Table I. In general, the value of the saturation intensities is defined by the absorption cross section and relaxation times. In tBLG with small twist angles the band structure is very complex. It consists of multiple flat moiré subbands and variation of the Fermi-level position makes possible both the optical transitions within different subbands (indirect transitions) as well as between them (direct transitions). The carriers in these bands have different masses and are characterized by different relaxation times. Changes in these parameters modify both, the absorption cross section and relaxation times, which affect the saturation intensities. Furthermore, probabilities of direct interband/intersubband transitions are proportional to the difference in occupations of the corresponding initial and final states, which depends on the Fermi energy position, i.e., the effective gate voltage. These arguments explain why the saturation intensities for different gate voltages vary strongly (from several to tens of kW/ cm^2) but not monotonically.

For negative gate voltages for which both amplitudes A^{ib} and A^{Dr} have the same sign, and for large positive gate voltages at which the Drude PGE dominates, the sign inversion with the increase in the radiation intensity is not detected and the photocurrent saturates with saturation intensities depending on the gate voltage.

The data discussed above are obtained at $T = 4$ K. Measurements for higher temperatures performed for several characteristic gate voltages demonstrated that up to about $T = 100$ K the photocurrent magnitude and its nonlinearity does not change much, see Fig. 4. This shows that the Drude absorption, being sensitive to the carrier scattering time, remains almost the same in this temperature range. Indeed, in transport measurements we observed that the sample resistance and, consequently, the momentum scattering time does not change much in this temperature range. At room temperatures, however, the overall behavior of the PGE changes substantially. First of all, no oscillations of the photocurrent upon variation of the gate voltages can be resolved, see Fig. 5. This is not surprising, considering that the forbidden gaps and used photon energies are on the order of several meV, whereas for room-temperature $k_B T$ is substantially higher being about 26 meV, here k_B is the Boltzmann constant. Furthermore, the saturation intensities at room temperature are observed to be substantially higher than those at low temperatures. The increase in the saturation intensities is caused by the enhancement of the scattering by phonons at room temperature, which substantially reduces the relaxation times.

B. Nonlinear photoconductivity

Finally, we briefly discuss the observed photoconductivity. Alike the photogalvanic effects discussed in the previous section, the photoconductive response is related to different absorption mechanisms caused by indirect-, direct-intersubband, and direct interband optical transitions. In two former cases (Drude-like and intersubband absorption), the number of free carriers does not change and the radiation-induced change of the sample conductance is caused by electron gas heating and the associated change in the carrier mobility. For the Drude absorption the photoconductivity is described by $\Delta\sigma = en\,\Delta\mu_n$ for electrons and $\Delta\sigma = ep\,\Delta\mu_p$ for holes, where μ_n and μ_p are electron and hole mobilities in the moiré subbands. For scattering by acoustic phonons the heating results in a negative photoconductivity, i.e., the conductivity decreases. This behavior is also reflected in the increase in the sample resistance with increasing temperature, see Fig. 8 in the Appendix. In contrast to the photocurrent, the sign of the photoconductivity does not depend on the type of carriers. At direct intersubband optical transitions THz radiation excites free carriers in the upper lying moiré subband. This process also results in a change in the conductivity because different moiré subbands may have different mobilities. On the other hand, absorption of radiation results in electron gas heating, and, as addressed above, in the change in μ_n or μ_p. In the case of direct optical transitions between the valence and conduction bands, THz radiation results in the generation of electron-hole pairs and, consequently, increases the sample conductance (positive photoconductivity). The opposite sign of the photoconductive response caused by the Drude- and interband contributions explains the sign inversions as a function of the gate voltage, which are observed at 4 K in the vicinity of the CNP, see Fig. 6 [71].

At the CNP, at which the Fermi level lies in the forbidden gap, the interband transitions yield the positive photoconductivity which dominates the photoresponse. An increase in $|U_{G,eff}|$ decreases this contribution as the difference between the population of the initial and final states decreases. However, an increase in $|U_{G,eff}|$ increases the Drude absorption and the magnitude of the corresponding negative photoconductivity. Consequently, the sign of the photoresponse reverses.

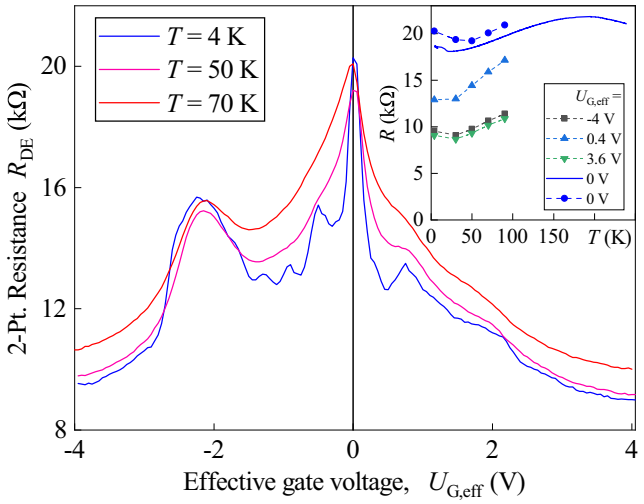

FIG. 8. Dependencies of the two-terminal resistance R_{DE} on the effective gate voltage $U_{G,eff}$ for different temperatures. The inset shows R_{DE} at various gate voltages as a function of the temperature.

At further increase in the gate voltages the photoresponse exhibits a resonancelike behavior and the sign reverses again, see Fig. 6. The resonances, marked in the figure by downward arrows, are caused by the direct intersubband transitions. Figure 6 reveals that these transitions yield the positive photoconductivity (THz radiation decreases the sample resistance).

Whereas the oscillations of the photoconductance are clearly detected up to rather high temperatures ($T \approx 100$ K), an increase in temperature results in the disappearance of the sign inversions, see Fig. 7. The temperature dependence of the photoconductivity measured at different gate voltages (at signal maximum, high positive/negative voltages and low positive gate voltages) shows that the lowest temperature inversion values are detected at high gate voltages of both polarities ($U_{\mathrm{G,eff}} < -3$ V and $U_{\mathrm{G,eff}} > 2$ V). These conditions correspond to the Drude mechanism being the dominant mechanism for the photoconductivity. The opposite signs of the photoconductive response detected for $T = 4$ and $T > 40$ K we attribute to the change in the temperature dependence of the carrier mobility and, consequently, the signs of $\Delta\mu_p$ and $\Delta\mu_n$. Note that the change in sign of $\partial R/\partial T$ is also detected in the transport measurements (not shown). Understanding the observed temperature sign inversion requires further studies and is out of scope of this paper.

Alike the photocurrent, the photoconductive signal saturates with increasing of the radiation intensity, see the inset in Fig. 6. Taking into account the nonlinearity of the corresponding absorbance [see Eqs. (2) and (3)] the nonlinearity of the total photoconductivity is described by

$$\frac{\Delta\sigma}{\sigma} = B^{\mathrm{Dr}} I \left(1 + \frac{I}{I_{\mathrm{s}}^{\mathrm{Dr}}}\right)^{-1} + B^{\mathrm{ib}} I \left(1 + \frac{I}{I_{\mathrm{s}}^{\mathrm{ib}}}\right)^{-1/2}, \quad (5)$$

with fitting parameters B^{Dr}, $I_{\mathrm{s}}^{\mathrm{Dr}}$, B^{ib}, and $I_{\mathrm{s}}^{\mathrm{ib}}$. Here B^{Dr} and B^{ib} are low-intensity amplitudes of the photoconductivity responses caused by indirect and direct optical transitions, respectively. For $T = 4$ K we observed that the amplitude B^{Dr} is negative and B^{ib} is positive. The inset in Fig. 6 shows that the above equation describes well the nonlinear behavior of the photoconductivity. The inset also shows that the decrease in the radiation frequency results in a substantial increase in the photoconductive signal. The increase in the absorption cross section with the reduction of frequency should result in a decrease in the saturation intensity, which is indeed detected in the experiment, see the inset in Fig. 6.

Note that the change in photon energy and gate voltage result in different kinds of optical transitions involving different subbands defining the variation of the signal amplitude upon changing the radiation frequency in tBLG. In the vicinity of the CNP we mostly deal with interband transitions, whereas at higher gate voltages an interplay of direct optical transitions between moiré subbands and Drude absorption within different subbands becomes important. The moiré subbands have different masses and the electron scattering times within these subbands can also be different. Therefore, deriving an analytical equation describing the frequency dependence of the signal is a challenging task and presenting the variation of the signal upon change in frequency is not informative.

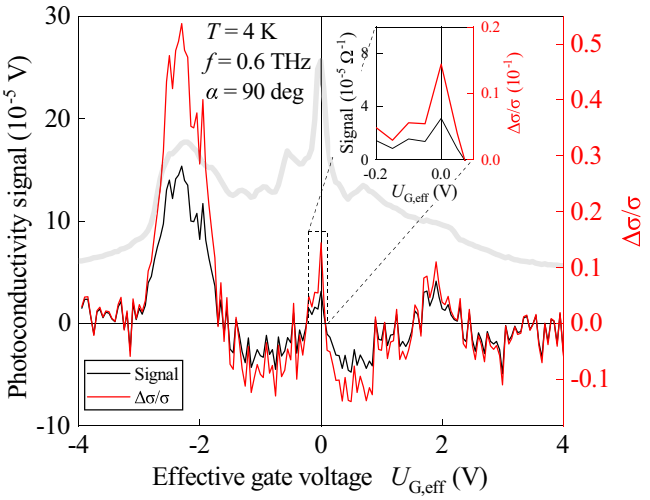

FIG. 9. Comparison of the gate voltage dependence of the photoconductivity signal (black) and the photoconductivity normalized on the conductivity $\Delta\sigma/\sigma$ (red) at a radiation frequency of 0.6 THz. The inset shows a zoom-in around the CNP.

V. SUMMARY

To summarize, the observed nonlinear intensity dependence of the THz radiation-induced bulk photogalvanic current can be well described by the interplay of two microscopic mechanisms related to the Drude-like free carrier absorption and direct interband/intersubband optical transitions. Both types of the photocurrent saturate at high intensities and are characterized by different values of their magnitudes and saturation intensities. Whereas the photocurrent related to the free-carrier absorption is generated at all gate voltages apart from the CNP at which it changes the sign, the photocurrent related to the direct optical transitions is only present for specific gate voltages corresponding to the maxima of the sample resistance. The observed saturation of the Drude contribution is attributed to the electron gas heating, whereas the one excited by the direct optical transitions is caused by the slow energy relaxation of the photoexcited carriers. Due to the complex band structures the magnitudes and the saturation intensities of the photocurrent varies nonmonotonically with the gate voltage. The excitation with intense terahertz radiation also results in a change of the tBLG conductivity which is related to different absorption channels. On one hand, the photoconductivity due to free-carrier absorption is caused by electron gas heating resulting in the change in the carrier mobility. On the other hand, the photoconductive response is excited due to direct interband transitions and direct optical transitions between moiré subbands. The direct optical transitions result in the resonancelike behavior of the photoconductivity as a function of the gate voltage. The interplay of all three contributions results in sign-alternating oscillations of the photoresponse with extrema positions corresponding to that of the sample resistance and the photogalvanic current. Alike the photogalvanic current, the photoconductive response saturates at high intensities, which is also caused by the nonlinearity of the radiation absorption. The observed saturation of the photocurrent and photoconductive response

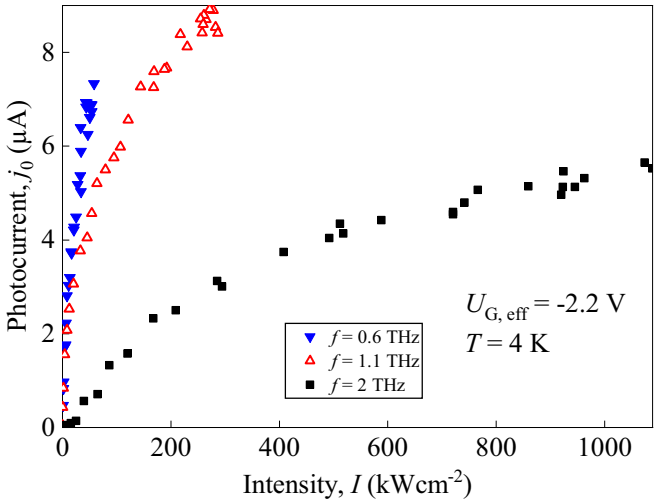

FIG. 10. Dependences of the polarization-independent photocurrent contribution in the y direction (see the inset in Fig. 1) on the radiation intensity for the radiation frequencies of 0.6, 1.1, and 2 THz at an effective gate voltage of $U_{G,\text{eff}} = -2.2$ V.

provide an access to study of scattering processes in twisted graphene with small twist angles close to the magic angle.

ACKNOWLEDGMENTS

We thank V. V. Bel'kov, D. Weiss, and L. E. Golub for fruitful discussions. The support from the Deutsche Forschungsgemeinschaft (DFG, German Research Foundation)—Project SPP 2244 (Project No. GA501/17-1), and the Volkswagen Stiftung Program (Program No. 97738) is gratefully acknowledged. S.D.G. acknowledges support from the IRAP Program of the Foundation for Polish Science (Grant No. MAB/2018/9, Project CENTERA). D.K.E. acknowledges support from the Ministry of Economy and Competitiveness of Spain through the "Severo Ochoa" Programme for Centres of Excellence in R and D (Program No. SE5-0522), Fundacio Privada Cellex, Fundacio Privada Mir-Puig, the Generalitat de Catalunya through the CERCA Programme, funding from the European Research Council (ERC) under the European Union's Horizon 2020 research and innovation Programme (Grant Agreement No. 852927). K.W. and T.T. acknowledge support from the Elemental Strategy Initiative conducted by the MEX, Japan (Grant No. JPMXP0112101001) and JSPS KAKENHI (Grants No. 19H05790, 20H00354 and No. 21H05233). G.D.B. acknowledges financial support from MCIN/AEI/ 10.13039/501100011033 and FSE "El FSE invierte en tu futuro" (Aid No. PRE2019-088487)

APPENDIX

1. Temperature evolution of resistance

Figure 8 shows the dependence of the samples resistance on the effective gate voltage for three different temperatures. The temperature evolution of the sample resistance for three effective gate voltages is plotted in the inset. Here, we also plotted the change in the resistance at zero gate voltage obtained at cooling down the sample, see the blue line. The data demonstrate that in the large range of temperatures from about 20 to 100 K the sample resistance increases with increasing temperature ($dR/dT > 0$) and decreases at higher temperatures with rising T ($dR/dT < 0$). The measured increase inf the sample resistance with the temperature is in line with the negative photoconductivity presented, e.g., in Fig. 6. Here, THz radiation-induced electron gas heating results in a rising electron temperature yielding an increased resistance and, consequently, a negative photoconductivity. Note that the temperature dependence of $\Delta\sigma/\sigma$ in Fig. 6 is presented for rather high intensities at which the electron gas heating is already strong. Therefore, despite that at $T = 4$ K the dark resistance decreases with the temperature, see the inset in Fig. 8, we detected a negative photoconductivity, which is expected at higher temperature. Furthermore, the change in the sign of dR/dT should result in the change in the photoconductivity sign, which is detected in experiment, see the inset in Fig. 7.

2. Comparison of photoconductivity signal and photoconductivity normalized to sample conductivity $\Delta\sigma/\sigma$

Figure 9 exemplary shows the gate voltage dependence of the normalized photoconductivity $\Delta\sigma/\sigma$ (red) and the photoconductive signal (black) for a radiation frequency of 0.6 THz. The figure demonstrates that the qualitative behavior is retained by the normalization, whereas there are differences in the relative amplitudes. Furthermore, it is shown that the signal, and, respectively, $\Delta\sigma$ itself (not the normalized one) clearly shows pronounced peaks and almost the same qualitative behavior as the normalized $\Delta\sigma/\sigma$. This is despite f the fact that the denominator σ in $\Delta\sigma/\sigma$ becomes small at resistance maxima. Whereas the resistance exhibits pronounced oscillations, its magnitude does not change much, therefore, normalization only slightly decreases the relative maxima amplitudes of $\Delta\sigma/\sigma$.

3. Frequency dependence of photocurrent

In Fig. 10 the polarization-independent photocurrent contribution j_0 is plotted as a function of the radiation intensity for the frequencies of 0.6, 1.1, and 2 THz at an effective gate voltage of $U_{G,\text{eff}} = -2.2$ V. It reveals that a decrease in radiation frequency leads to an increase in the photocurrent magnitude and to a decrease in the saturation intensity.

[1] Y. Cao, V. Fatemi, A. Demir, S. Fang, S. L. Tomarken, J. Y. Luo, J. D. Sanchez-Yamagishi, K. Watanabe, T. Taniguchi, E. Kaxiras, R. C. Ashoori, and P. Jarillo-Herrero, Nature (London) **556**, 80 (2018).

[2] Y. Cao, V. Fatemi, S. Fang, K. Watanabe, T. Taniguchi, E. Kaxiras, and P. Jarillo-Herrero, Nature (London) **556**, 43 (2018).

[3] F. Wu, A. H. MacDonald, and I. Martin, Phys. Rev. Lett. **121**, 257001 (2018).

[4] H. C. Po, L. Zou, A. Vishwanath, and T. Senthil, Phys. Rev. X **8**, 031089 (2018).

[5] C. Xu and L. Balents, Phys. Rev. Lett. **121**, 087001 (2018).

[6] M. Yankowitz, S. Chen, H. Polshyn, Y. Zhang, K. Watanabe, T. Taniguchi, D. Graf, A. F. Young, and C. R. Dean, Science **363**, 1059 (2019).

[7] X. Lu, P. Stepanov, W. Yang, M. Xie, M. A. Aamir, I. Das, C. Urgell, K. Watanabe, T. Taniguchi, G. Zhang, A. Bachtold, A. H. MacDonald, and D. K. Efetov, Nature (London) **574**, 653 (2019).

[8] C. Shen, Y. Chu, Q. Wu, N. Li, S. Wang, Y. Zhao, J. Tang, J. Liu, J. Tian, K. Watanabe, T. Taniguchi, R. Yang, Z. Y. Meng, D. Shi, O. V. Yazyev, and G. Zhang, Nat. Phys. **16**, 520 (2020).

[9] X. Liu, Z. Hao, E. Khalaf, J. Y. Lee, Y. Ronen, H. Yoo, D. H. Najafabadi, K. Watanabe, T. Taniguchi, A. Vishwanath, and P. Kim, Nature (London) **583**, 221 (2020).

[10] A. L. Sharpe, E. J. Fox, A. W. Barnard, J. Finney, K. Watanabe, T. Taniguchi, M. A. Kastner, and D. Goldhaber-Gordon, Science **365**, 605 (2019).

[11] G. Li, A. Luican, J. M. B. Lopes dos Santos, A. H. Castro Neto, A. Reina, J. Kong, and E. Y. Andrei, Nat. Phys. **6**, 109 (2009).

[12] W. Yan, M. Liu, R.-F. Dou, L. Meng, L. Feng, Z.-D. Chu, Y. Zhang, Z. Liu, J.-C. Nie, and L. He, Phys. Rev. Lett. **109**, 126801 (2012).

[13] A. Mishchenko, J. S. Tu, Y. Cao, R. V. Gorbachev, J. R. Wallbank, M. T. Greenaway, V. E. Morozov, S. V. Morozov, M. J. Zhu, S. L. Wong, F. Withers, C. R. Woods, Y.-J. Kim, K. Watanabe, T. Taniguchi, E. E. Vdovin, O. Makarovsky, T. M. Fromhold, V. I. Fal'ko, A. K. Geim *et al.*, Nat. Nanotechnol. **9**, 808 (2014).

[14] J. M. B. Lopes dos Santos, N. M. R. Peres, and A. H. Castro Neto, Phys. Rev. Lett. **99**, 256802 (2007).

[15] E. S. Morell, J. D. Correa, P. Vargas, M. Pacheco, and Z. Barticevic, Phys. Rev. B **82**, 121407(R) (2010).

[16] E. J. Mele, Phys. Rev. B **81**, 161405(R) (2010).

[17] R. Bistritzer and A. H. MacDonald, Proc. Natl. Acad. Sci. USA **108**, 12233 (2011).

[18] A. Luican, G. Li, A. Reina, J. Kong, R. R. Nair, K. S. Novoselov, A. K. Geim, and E. Y. Andrei, Phys. Rev. Lett. **106**, 126802 (2011).

[19] A. Rozhkov, A. Sboychakov, A. Rakhmanov, and F. Nori, Phys. Rep. **648**, 1 (2016).

[20] K. Kim, A. DaSilva, S. Huang, B. Fallahazad, S. Larentis, T. Taniguchi, K. Watanabe, B. J. LeRoy, A. H. MacDonald, and E. Tutuc, Proc. Natl. Acad. Sci. USA **114**, 3364 (2017).

[21] M. Koshino, N. F. Q. Yuan, T. Koretsune, M. Ochi, K. Kuroki, and L. Fu, Phys. Rev. X **8**, 031087 (2018).

[22] R. Ribeiro-Palau, C. Zhang, K. Watanabe, T. Taniguchi, J. Hone, and C. R. Dean, Science **361**, 690 (2018).

[23] H. Yoo, R. Engelke, S. Carr, S. Fang, K. Zhang, P. Cazeaux, S. H. Sung, R. Hovden, A. W. Tsen, T. Taniguchi, K. Watanabe, G.-C. Yi, M. Kim, M. Luskin, E. B. Tadmor, E. Kaxiras, and P. Kim, Nature Mater. **18**, 448 (2019).

[24] A. Kerelsky, L. J. McGilly, D. M. Kennes, L. Xian, M. Yankowitz, S. Chen, K. Watanabe, T. Taniguchi, J. Hone, C. Dean, A. Rubio, and A. N. Pasupathy, Nature (London) **572**, 95 (2019).

[25] Y. Jiang, X. Lai, K. Watanabe, T. Taniguchi, K. Haule, J. Mao, and E. Y. Andrei, Nature (London) **573**, 91 (2019).

[26] M. Serlin, C. L. Tschirhart, H. Polshyn, Y. Zhang, J. Zhu, K. Watanabe, T. Taniguchi, L. Balents, and A. F. Young, Science **367**, 900 (2020).

[27] M. Xie and A. H. MacDonald, Phys. Rev. Lett. **124**, 097601 (2020).

[28] P. Stepanov, I. Das, X. Lu, A. Fahimniya, K. Watanabe, T. Taniguchi, F. H. L. Koppens, J. Lischner, L. Levitov, and D. K. Efetov, Nature (London) **583**, 375 (2020).

[29] Y. Cao, D. Chowdhury, D. Rodan-Legrain, O. Rubies-Bigorda, K. Watanabe, T. Taniguchi, T. Senthil, and P. Jarillo-Herrero, Phys. Rev. Lett. **124**, 076801 (2020).

[30] X. Lu, B. Lian, G. Chaudhary, B. A. Piot, G. Romagnoli, K. Watanabe, T. Taniguchi, M. Poggio, A. H. MacDonald, B. A. Bernevig, and D. K. Efetov, Proc. Natl. Acad. Sci. USA **118**, e2100006118 (2021).

[31] B. A. Bernevig, Z.-D. Song, N. Regnault, and B. Lian, Phys. Rev. B **103**, 205411 (2021).

[32] Y. Cao, D. Rodan-Legrain, J. M. Park, N. F. Q. Yuan, K. Watanabe, T. Taniguchi, R. M. Fernandes, L. Fu, and P. Jarillo-Herrero, Science **372**, 264 (2021).

[33] Z. Hao, A. M. Zimmerman, P. Ledwith, E. Khalaf, D. H. Najafabadi, K. Watanabe, T. Taniguchi, A. Vishwanath, and P. Kim, Science **371**, 1133 (2021).

[34] I. Das, X. Lu, J. Herzog-Arbeitman, Z.-D. Song, K. Watanabe, T. Taniguchi, B. A. Bernevig, and D. K. Efetov, Nat. Phys. **17**, 710 (2021).

[35] S. Wu, Z. Zhang, K. Watanabe, T. Taniguchi, and E. Y. Andrei, Nature Mater. **20**, 488 (2021).

[36] Y. Choi, J. Kemmer, Y. Peng, A. Thomson, H. Arora, R. Polski, Y. Zhang, H. Ren, J. Alicea, G. Refael, F. von Oppen, K. Watanabe, T. Taniguchi, and S. Nadj-Perge, Nat. Phys. **15**, 1174 (2019).

[37] M. Otteneder, S. Hubmann, X. Lu, D. A. Kozlov, L. E. Golub, K. Watanabe, T. Taniguchi, D. K. Efetov, and S. D. Ganichev, Nano Lett. **20**, 7152 (2020).

[38] W. Xin, X.-D. Chen, Z.-B. Liu, W.-S. Jiang, X.-G. Gao, X.-Q. Jiang, Y. Chen, and J.-G. Tian, Adv. Opt. Mater. **4**, 1703 (2016).

[39] J. Yin, H. Wang, H. Peng, Z. Tan, L. Liao, L. Lin, X. Sun, A. L. Koh, Y. Chen, H. Peng, and Z. Liu, Nat. Commun. **7**, 10699 (2016).

[40] S. S. Sunku, A. S. McLeod, T. Stauber, H. Yoo, D. Halbertal, G. Ni, A. Sternbach, B.-Y. Jiang, T. Taniguchi, K. Watanabe, P. Kim, M. M. Fogler, and D. N. Basov, Nano Lett. **20**, 2958 (2020).

[41] N. C. H. Hesp, I. Torre, D. Barcons-Ruiz, H. H. Sheinfux, K. Watanabe, T. Taniguchi, R. K. Kumar, and F. H. L. Koppens, Nat. Commun. **12**, 1640 (2021).

[42] S. S. Sunku, D. Halbertal, T. Stauber, S. Chen, A. S. McLeod, A. Rikhter, M. E. Berkowitz, C. F. B. Lo, D. E. Gonzalez-Acevedo, J. C. Hone, C. R. Dean, M. M. Fogler, and D. N. Basov, Nat. Commun. **12**, 1641 (2021).

[43] G. Di Battista, P. Seifert, K. Watanabe, T. Taniguchi, K. C. Fong, A. Principi, D. K. Efetov, arXiv:2111.08735.

[44] Q. Bao, H. Zhang, Y. Wang, Z. Ni, Y. Yan, Z. X. Shen, K. P. Loh, and D. Y. Tang, Adv. Funct. Mater. **19**, 3077 (2009).

[45] P. Avouris and F. Xia, MRS Bull. **37**, 1225 (2012).

[46] L. Turyanska, O. Makarovsky, S. A. Svatek, P. H. Beton, C. J. Mellor, A. Patanè, L. Eaves, N. R. Thomas, M. W. Fay, A. J. Marsden, and N. R. Wilson, Adv. Electron. Mater. **1**, 1500062 (2015).

[47] V. Bianchi, T. Carey, L. Viti, L. Li, E. H. Linfield, A. G. Davies, A. Tredicucci, D. Yoon, P. G. Karagiannidis, L. Lombardi, F. Tomarchio, A. C. Ferrari, F. Torrisi, and M. S. Vitiello, Nat. Commun. **8**, 15763 (2017).

[48] A. D. Sanctis, J. Mehew, M. Craciun, and S. Russo, Materials **11**, 1762 (2018).

[49] A. Autere, H. Jussila, Y. Dai, Y. Wang, H. Lipsanen, and Z. Sun, Adv. Mater. **30**, 1705963 (2018).

[50] J. W. You, S. R. Bongu, Q. Bao, and N. C. Panoiu, Nanophotonics **8**, 63 (2018).

[51] M. Mittendorff, S. Winnerl, and T. E. Murphy, Adv. Opt. Mater. **9**, 2001500 (2020).

[52] L. Wang, I. Meric, P. Y. Huang, Q. Gao, Y. Gao, H. Tran, T. Taniguchi, K. Watanabe, L. M. Campos, D. A. Muller, J. Guo, P. Kim, J. Hone, K. L. Shepard, and C. R. Dean, Science **342**, 614 (2013).

[53] S. Candussio, M. V. Durnev, S. Slizovskiy, T. Jötten, J. Keil, V. V. Bel'kov, J. Yin, Y. Yang, S.-K. Son, A. Mishchenko, V. Fal'ko, and S. D. Ganichev, Phys. Rev. B **103**, 125408 (2021).

[54] K.-M. Dantscher, D. A. Kozlov, M. T. Scherr, S. Gebert, J. Bärenfänger, M. V. Durnev, S. A. Tarasenko, V. V. Bel'kov, N. N. Mikhailov, S. A. Dvoretsky, Z. D. Kvon, J. Ziegler, D. Weiss, and S. D. Ganichev, Phys. Rev. B **95**, 201103(R) (2017).

[55] V. A. Shalygin, H. Diehl, C. Hoffmann, S. N. Danilov, T. Herrle, S. A. Tarasenko, D. Schuh, C. Gerl, W. Wegscheider, W. Prettl, and S. D. Ganichev, JETP Lett. **84**, 570 (2007).

[56] H. Plank, L. E. Golub, S. Bauer, V. V. Bel'kov, T. Herrmann, P. Olbrich, M. Eschbach, L. Plucinski, C. M. Schneider, J. Kampmeier, M. Lanius, G. Mussler, D. Grützmacher, and S. D. Ganichev, Phys. Rev. B **93**, 125434 (2016).

[57] S. D. Ganichev, P. Schneider, V. V. Bel'kov, E. L. Ivchenko, S. A. Tarasenko, W. Wegscheider, D. Weiss, D. Schuh, B. N. Murdin, P. J. Phillips, C. R. Pidgeon, D. G. Clarke, M. Merrick, P. Murzyn, E. V. Beregulin, and W. Prettl, Phys. Rev. B **68**, 081302(R) (2003).

[58] S. Hubmann, S. Gebert, G. V. Budkin, V. V. Bel'kov, E. L. Ivchenko, A. P. Dmitriev, S. Baumann, M. Otteneder, J. Ziegler, D. Disterheft, D. A. Kozlov, N. N. Mikhailov, S. A. Dvoretsky, Z. D. Kvon, D. Weiss, and S. D. Ganichev, Phys. Rev. B **99**, 085312 (2019).

[59] S. Candussio, L. E. Golub, S. Bernreuter, T. Jötten, T. Rockinger, K. Watanabe, T. Taniguchi, J. Eroms, D. Weiss, and S. D. Ganichev, Phys. Rev. B **104**, 155404 (2021).

[60] V. V. Bel'kov, S. D. Ganichev, E. L. Ivchenko, S. A. Tarasenko, W. Weber, S. Giglberger, M. Olteanu, H.-P. Tranitz, S. N. Danilov, P. Schneider, W. Wegscheider, D. Weiss, and W. Prettl, J. Phys.: Condens. Matter **17**, 3405 (2005).

[61] Note that the highest intensities applied scale from about $50\mathrm{kW/cm^2}$ to $1\mathrm{MW/cm^2}$ depending on the radiation frequency, which is caused by the line-dependent laser power limit.

[62] S. D. Ganichev, S. N. Danilov, V. V. Bel'kov, E. L. Ivchenko, M. Bichler, W. Wegscheider, D. Weiss, and W. Prettl, Phys. Rev. Lett. **88**, 057401 (2002).

[63] S. N. Danilov, L. E. Golub, T. Mayer, A. Beer, S. Binder, E. Mönch, J. Minár, M. Kronseder, C. H. Back, D. Bougeard, and S. D. Ganichev, Phys. Rev. Appl. **16**, 064030 (2021).

[64] Note that in the vicinity of CNP we obtain direct optical transitions between valence and conduction bands, which consequently result in the generation of electron-hole pairs. For higher gate voltages, however, direct optical transitions appear between moiré subbands and result in a photoexcitation of free carriers.

[65] Z. Mics, K.-J. Tielrooij, K. Parvez, S. A. Jensen, I. Ivanov, X. Feng, K. Müllen, M. Bonn, and D. Turchinovich, Nat. Commun. **6**, 7655 (2015).

[66] N. V. Leppenen and L. E. Golub, arXiv:2110.15236.

[67] N. V. Leppenen, E. L. Ivchenko, and L. E. Golub, Phys. Status Solidi B **256**, 1900305 (2019).

[68] W. Demtröder, *Laser Spectroscopy*, 4th ed. (Springer, Berlin/Heidelberg, 2008), Vol. 2.

[69] S. D. Ganichev and W. Prettl, *Intense Terahertz Excitation of Semiconductors* (Oxford University Press, Oxford, 2005).

[70] Note that the second contribution of the linear photogalvanic effect given by the coefficient j_2 is almost zero, which excludes study of its nonlinearity.

[71] Note that the cool-down-dependent shift of the CNP detected in transport measurements indicates that surface charges may affect the results close to the CNP. This generally may result in a photoexcited shift of the CNP [46]. This effect, however, is unlikely at THz frequencies due to low energy (at $f = 0.6\mathrm{THz}$ photon energy is 2.5 meV). Indeed, the peak of the photoconductive signal is at almost the same gate voltage as the peak of resistance at the CNP, see Fig. 6.